Pergamon

Geochimica et Cosmochimica Acta, Vol. 66, No. 4, pp. 561–576, 2002

0016-7037/−1898 $22.00 + .00

PII S0016-7037(01)00778-5

Analysis of individual fluid inclusions using Synchrotron X-Ray Fluorescence microprobe: progress toward calibration for trace elements

BÉNÉDICTE MÉNEZ,[1,2,*] PASCAL PHILIPPOT,[2] MICHELLE BONNIN-MOSBAH,[1] ALEXANDRE SIMIONOVICI,[3] and FRANÇOIS GIBERT[4]

[1]Laboratoire Pierre Süe, CEA-CNRS, Batiment 637, C. E. Saclay, 91191 Gif Sur Yvette cedex, France
[2]Laboratoire de Géosciences Marines, CNRS-FRE 2316, Institut de Physique du Globe, case 89, T26-00 E3, 4 place Jussieu, 75252 Paris cedex 05, France
[3]European Synchrotron Radiation Facility, μFID group, ID22, BP 220, 38043 Grenoble cedex, France
[4]CNRS, UMR 6524, Université Blaise Pascal, 63038 Clermont Ferrand, France

(*Received February* 15, 2000; *accepted in revised form July* 17, 2001)

Abstract—A critical problem for conducting quantitative analysis of individual fluid inclusions using Synchrotron X-Ray Fluorescence (SXRF) technique relates to the standardization and the calibration of the X-ray spectra. In this study, different approaches have been tested for calibration purposes: (a) the use of chlorine when Cl content can be estimated either from melting point depressions of undersaturated fluid inclusions or from saturation limits for halite-bearing fluid inclusions, (b) the use of calcium from synthetic fluid inclusions of known $CaCl_2$ content as an external standard. SXRF analysis was performed on individual fluid inclusions from the Chivor and Guali emerald deposits, Columbia. These well-known samples contain a single fluid inclusion population for which detailed crush-leach analyses are available, thus providing a relevant compositional reference frame. Concentration estimates were also compared to Particle Induced X-ray Emission (PIXE) analysis carried out independently on the same fluid inclusions.

Results of the calibration tests indicate that major (Cl, K, Ca, Fe, Mn) and trace element (Cu, Zn, As, Br, Rb, Sr, Ba, Pb) concentration estimates can be performed without precise knowledge of the analytical volume and the inclusion's 3D geometry. Although the standard deviation of the SXRF results can be relatively high depending on the calibration mode used, mean concentration estimates for most elements are in good agreement with PIXE and crush-leach analysis. Elemental distributions within single fluid inclusions were also established. Associated correlation diagrams argue for the homogeneous distribution of most elements in the fluid inclusion. In contrast, Br shows a bimodal distribution interpreted to reflect a significant enrichment of the vapor portion of the inclusion fluid.

1. INTRODUCTION

Fluid inclusions represent the only direct samples of ancient fluids in many crustal rocks. They are considered to be representative of the fluid present during either the growth of minerals or the later healing of fluid-filled cracks. Accordingly, their composition provides crucial information for studies of fluid–rock interactions. Many natural minerals contain several generations of fluid inclusions, each one being representative of a distinct hydrothermal event. Therefore, there is general recognition of the uncertainties inherent in bulk analytical approaches such as crush-leach analysis, which result in homogenizing several fluid populations.

The potential of Synchrotron X-Ray Fluorescence (SXRF) microprobe for conducting quantitative analysis of single fluid inclusions has recently been recognized (Frantz et al., 1988; Rankin et al., 1992; Vanko et al., 1993, 2001; Bodnar et al., 1995; Bühn and Rankin, 1999; Cline and Vanko, 1995; Mavrogenes et al., 1995; Philippot et al., 1995, 1998, 2000, 2001; Ménez et al., 1998a,b; Ménez, 1999; Vanko and Mavrogenes, 1998). The advantages of this technique remain its non destructive character, a high spatial resolution, and the in situ multi-element analytical capability. Moreover, the recent development of third-generation synchrotron radiation sources has opened up the prospect of a highly sensitive instrument with potential sub-ppm detection limits (e.g., Chevallier et al., 1996).

Previous studies have demonstrated the efficiency of the SXRF technique for the detection of ionic species in synthetic and natural fluid inclusions (see Vanko and Mavrogenes, 1998 for a recent review). However, the computational procedures used to estimate the elemental concentrations present two major difficulties and, as a consequence, alternative approaches are needed to improve on these estimates. First, corrections for X-ray self-absorption by the inclusion fluid and the host mineral are required. Previous research has relied on optical techniques for estimating the pathlengths traversed by the incident beam and the fluorescent radiation through host mineral and fluid. Philippot et al. (1998) showed that the $K\alpha/K\beta$ ratio of an element present in solution is directly related to the thickness of material traversed by the radiation, thus providing improved pathlength estimates commonly better than ± 1 μm Philippot et al., 1998, 2001). A similar approach can be found in Ryan et al. (1991, 1993) for identical problems in Particle-Induced X-ray Emission (PIXE) analysis.

The other limiting factor associated with SXRF analysis concerns the standardization of the measurements. Calibration of the collected element X-ray intensities remains a major problem. As a consequence, most attempts display qualitative results (Bodnar et al., 1995) or semi-quantitative analysis yielding elemental ratios (Rankin et al., 1992; Vanko et al., 1993; Philippot et al., 1995; Vanko and Mavrogenes, 1998). For

* Author to whom correspondence should be addressed (menez@ipgp.jussieu.fr).

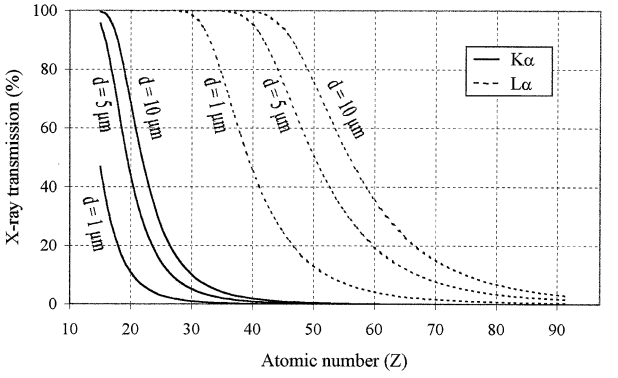

Fig. 1. X-ray transmission versus atomic number for different quartz thicknesses (d) above fluid inclusion (respectively 1, 5, and 10 μm). Note that low-energy X-rays associated with low-Z elements ($Z < 25$) for Kα X-rays and medium-Z elements ($40 < Z < 60$) for Lα X-rays, respectively, are very sensitive to the fluid inclusion depth.

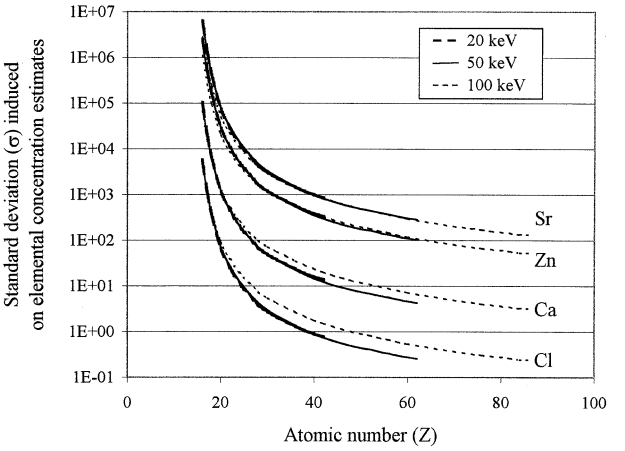

Fig. 2. Theoretical evolution of the standard deviation on elemental concentration estimates induced by a 30% uncertainty on the standard concentration. Several internal standards of different atomic number (Cl, Ca, Zn, Sr) are evaluated for different incident beam energies (20, 50, and 100 keV). Simulations were performed using a fluid inclusion depth of 10 μm and an internal standard concentration of 10,000 ppm. Owing to the high sensitivity of low-energy X-rays to absorption (see Fig. 1), the error induced on the calculated concentrations of the heaviest elements ($Z >$ Mn) is minimized using light elements such as Cl and Ca as internal standard. Particularly, in the case of Cl, the error propagation on element heavier than Fe reduces to 1% of the original uncertainty on Cl concentration.

quantitative analysis, the strategy may vary. In Frantz et al. (1988), Cline and Vanko (1995), and Vanko et al. (2001), concentrations were quantified using thin film standards of known composition. Mavrogenes et al. (1995) used silica-glass capillaries containing solutions of known concentrations. In all cases, a simplified fluid inclusion geometry, characterized by plate-parallel faces, is assumed for estimating fluorescence yield and self-absorption correction. These calibration procedures also require accurate fluid inclusion depth and volume estimates. In many cases the uncertainty of such estimates may cause significant errors, which affect severely the accuracy of the quantification. Philippot et al. (1998, 2001) used one of the elements present in solution as an internal standard, establishing that the Kα X-ray peak intensity of this element corresponds to a known concentration, determined by crush-leach analysis. However this approach requires dealing only with samples containing one population of fluid inclusions. The aim of this study was to establish calibration procedures, potentially appropriate to all samples, for conducting quantitative analysis of individual fluid inclusions.

2. ANALYTICAL STRATEGY

Two calibration procedures were evaluated here. First, when chlorine is detected in the SXRF spectrum, this element, which is ubiquitous in crustal fluids, can be used as an internal standard. For undersaturated fluid inclusions, Cl content is estimated from microthermometric experiments (salinity can be expressed in terms of equivalent wt.% NaCl) or, more precisely, determined directly using Raman spectroscopy technique (chlorinity, Mernagh and Wilde, 1989). For halite-bearing fluid inclusions, because analyses are systematically performed in the liquid phase of the inclusion, chlorine concentration is deduced from that of a 26 wt.% equivalent NaCl solution. However, as shown in Figure 1, low-energy X-ray yield (i.e., soft X-rays) is very sensitive to the depth of the analyzed fluid inclusion and the airpath between the specimen and the detector. As a result, X-rays of light elements are generally absorbed before reaching the detector. Accordingly, chlorine is not systematically detected using the SXRF technique, particularly for low salinity fluids. Alternatively, external standardization using synthetic fluid inclusions containing a known $CaCl_2$ content can be employed. This allows estimating, by comparison between the two analyses, the Ca concentration of the natural fluid inclusion. Ca can in turn be used as an internal standard for quantifying the other elements present in the X-ray spectrum.

A potential drawback of using Cl concentration estimates by freezing point depression or using saturation limits for halite-bearing inclusions lies in quoting Cl concentration in terms of NaCl equivalent. According to Crawford (1981), errors in estimating salinities for $CaCl_2$-rich solutions will be small but can reach up to 5 wt.% if the fluid has either a high KCl or high $MgCl_2$ content. For example, considering a maximum error of 5 wt.% salt of a saturated NaCl fluid results in an error of $\sim$20% on estimated Cl concentration.

The effects of introducing a significant error on Cl estimates on calculated element concentrations were evaluated. Figure 2 shows the theoretical evolution of the standard deviation on elemental concentration estimates induced by a 30% uncertainty on the standard content. Interestingly, note that, owing to the strong sensitivity of light elements to absorption (see Fig. 1), the propagated error on calculated concentrations of the heaviest elements ($Z >$ Mn) is minimized using light elements such as Cl and Ca as internal standard. As an example, the error propagation on element heavier than Mn reduces to $\sim$1% of the original standard deviation on Cl concentration (see Fig. 2).

To check the accuracy of the evaluated calibration procedures, SXRF analyses were performed in samples containing only a single compositional type of fluid inclusions previously characterized using a large variety of techniques, including crush-leach analysis (see section 3.1). Importantly, PIXE anal-

yses were carried out on the same fluid inclusions. Although based on similar physical processes, the photon and proton microprobes display complementary aspects. Of particular relevance is that for a given energy, X-ray production cross-sections are expressed as a function of Z^4 for SXRF and $1/Z^4$ for PIXE, Z corresponding to the atomic number of the target element. As a consequence, the nuclear microprobe is better suited for light element detection ($Z \leq 22$). Moreover, the nuclear microprobe, under vacuum, displays lower absorption for the light element X-rays. PIXE is therefore well adapted for evaluating the reliability of light element concentration estimates using SXRF.

3. ANALYZED SAMPLES

3.1. Results of Previous Studies

The fluid inclusions studied are from natural quartz-bearing rocks collected in the Chivor (sample GG20) and Guali (sample GG15) emerald deposits from Columbia (kindly provided by Gaston Giuliani). Those deposits are located within the eastern and western borders of the Eastern Cordillera (e.g., Giuliani et al., 1995). They define two mineralized zones hosted within Early Cretaceous black shales: the eastern zone with the mining districts of Chivor and Guali; the western zone containing the districts of Coscuez and Muzo. Emerald occurs within carbonate veins and breccia in black shales (Cheilletz and Giuliani, 1996). Fluids are predominantly Na-Cl-Fe-Ca-K-SO_4 brines and were derived from dissolution of primary halite-anhydrite (Banks et al., 1995). The source of beryllium is sedimentary and the sulfide-sulfur source is evaporitic (Ottaway et al., 1994; Giuliani et al., 1995). The emeralds display a pronounced enrichment in ^{18}O as do the carbonates. The calculated $\delta^{18}O$ of H_2O and measured δD of fluid inclusions for carbonates and emeralds are consistent with values of evolved basinal brines (Giuliani et al., 1997).

At room temperature, the inclusions consist of a liquid aqueous phase, a vapor phase, a large halite crystal, and additional undetermined daughter crystals. Table 1 shows the electrolyte composition determined by crush-leach analysis (Banks et al., 2000). Microthermometric measurements, performed by Gaston Giuliani, give average fluid inclusion salinities of 30.2 wt.% equivalent NaCl for sample GG20 and 40 wt.% equivalent NaCl for sample GG15.

Table 1. Reconstructed composition of quartz-hosted fluids determined using crush-leach analysis (Banks et al., 2000), in ppm.

	Chivor deposit (GG20)	Guali deposit (GG15)
Li	2,549	2,090
Be	1.2	0.48
Na	63,844	78,554
Mg	1,435	385
K	8,796	17,415
Ca	31,855	32,356
Mn	1,025	2,176
Fe	4,579	23,252
Cu	bd[a]	825
Zn	950	997
As	48	39
Ba	1,503	652
Pb	315	383
Sr	1,524	825
SO_4	bd[a]	614
Cl	183,208	242,078
Br	42.8	23.8
I	1.5	2.2

[a] Below detection.

3.2. Practical Aspects

Doubly polished chips of quartz of 30 to 100 μm thickness were used for measurements. Thin samples (down to 50 μm) allow minimizing the background of the X-ray spectrum arising from the photons scattered by the matrix, thus providing a

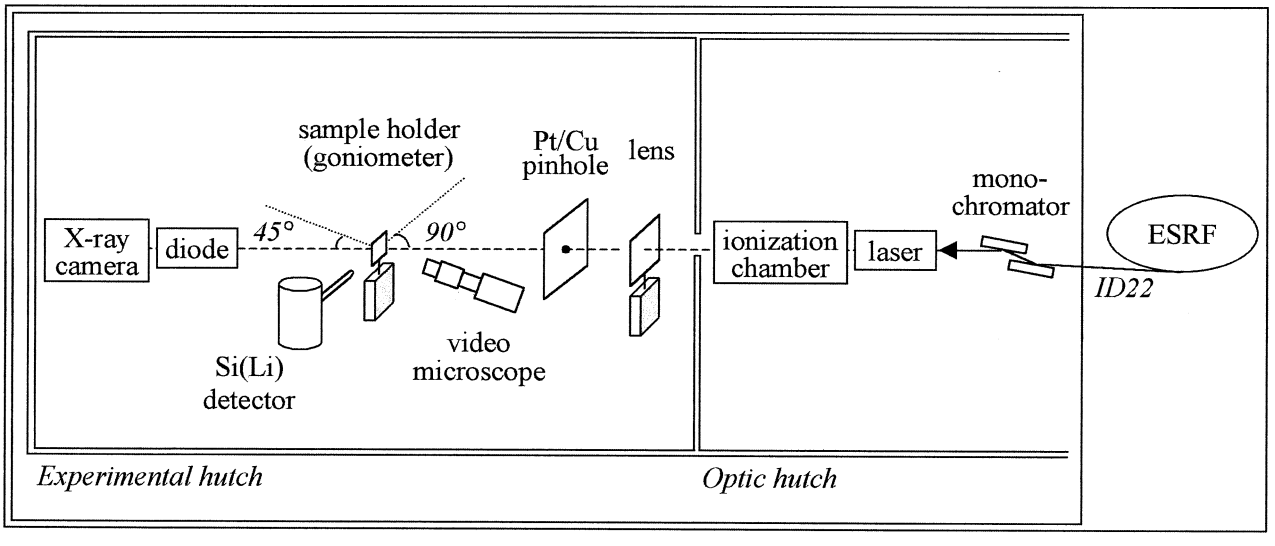

Fig. 3. X-ray microfluorescence setup installed on beamline ID22 of the ESRF, Grenoble, France. The lens corresponds to a Fresnel Zone Plate, using 15 keV incident energy, and a Compound Refractive Lens using 22 keV incident energy.

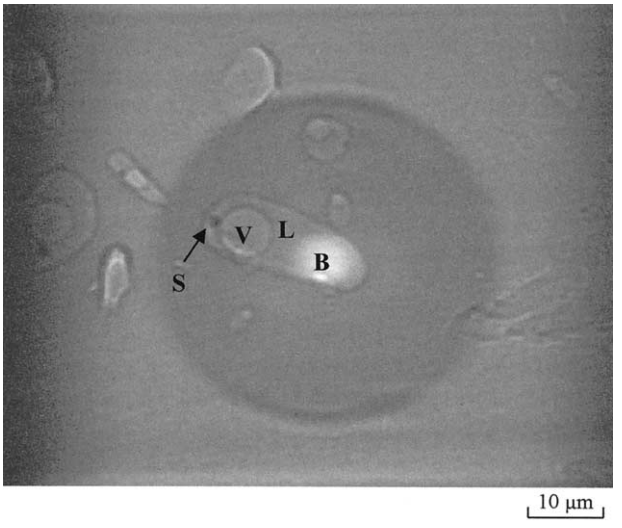

Fig. 4. Phase contrast image obtained with a CCD camera of 0.1 μm spatial resolution placed behind the sample. Note the photon beam (B) passing through the liquid phase (L) of the three phase fluid inclusion (V, vapor; S, solid)

better signal/background ratio and hence better sensitivity. Samples were washed in acetone in an ultrasonic bath to remove any traces of dust, resin, or polishing compounds. Suitable fluid inclusions were examined and selected in transmitted light before analysis. Because low-energy X-ray yields are very sensitive to host-mineral absorption, fluid inclusions have to be located near the sample surface ($<$15 μm). To target only the liquid portion, fluid inclusions must display a minimum size of 10 $\times$ 15 μm. Finally, because the photon beam penetrates the entire sample, it is necessary to choose isolated inclusions throughout the quartz chip.

4. EXPERIMENTAL SETUP

4.1. Micro-SXRF

The micro-SXRF measurements were performed on the microprobe installed on undulator beamline μFID (Fluorescence, Imaging, and Diffraction, ID22) of the European Synchrotron Radiation Facility (ESRF), a third-generation synchrotron light source. As illustrated in Figure 3, the radiation was monochromatized by a double crystal fixed-exit monochromator (Si [111] plane). A Fresnel Zone Plate (FZP) with high demagnification factor ensured the focusing of monochromatized X-rays at $\sim$15 keV, with a spatial resolution of 2 $\times$ 7 μm^2 and a flux of 5.10^9 photons per second. Experiments were also carried out using an incident energy of 22 keV impinging on a prefocusing Compound Refractive Lens (CRL; Snigirev, 1995; Snigirev et al., 1996). As these lenses display different focal distances, both can be installed in the beam path at different distances from the sample and then be used alternatively during the same experiment. Excitation energies (15 and 22 keV) were chosen to maximize the sensitivity of a wide range of elements from Ca to Pb. To restrict the scattered beam, a Pt/Cu pinhole of 10 μm diameter was positioned behind the Fresnel Zone Plate on 2-axis stage. The beam was monitored by current integration detectors (silicon PIN diode) and an ionization chamber. The

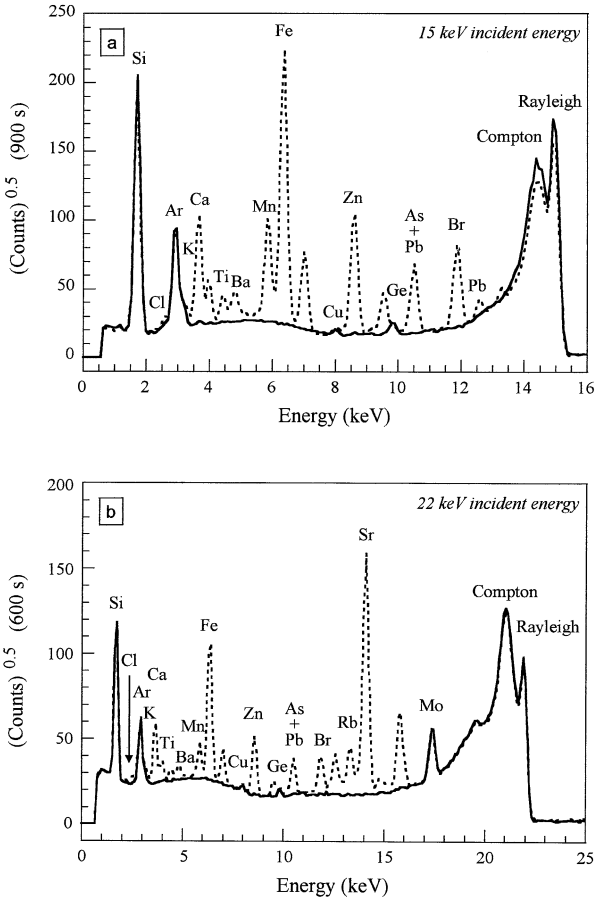

Fig. 5. SXRF spectra obtained on a single fluid inclusion (i.e., 6i′) from Chivor emerald deposit (Columbia), with 15 [3a] and 22 keV [3b] incident energy, respectively. Two spectra are overlaid: spectrum obtained on the fluid inclusion (broken line) and a control spectrum obtained in the nearby free-inclusion quartz (solid line). Rayleigh and Compton peaks represent the elastic and inelastic scattering of photons, respectively. The X-ray spectrum reveals the presence of Cl, K, Ca, Mn, Fe, Cu, Zn, As, Br, Rb, Sr, Ba, and Pb, well above the background noise and restricted solely to the inclusion. Si and Ge derived from the host quartz and Ar from the surrounding air. Mo and a part of Cu are emerging from the collimator placed in front of the detector Be window. The 22 keV incident energy displays a better sensitivity for the detection of heavier elements. Note how Sr, with a critical excitation energy of 16.1 keV, is observed in [5b] but is absent from [5a].

sample under investigation was positioned in the image plane with an accuracy of 0.1 μm with a three-axis (x, y, z) remote-controlled stage, set at 45° from the incident beam. The position of the focal spot was visualized using two perpendicular reticules on a color TV screen connected to a 700 magnification video microscope installed normal to the sample surface. X-ray fluorescence measurements were carried out with an energy-dispersive solid-state Si(Li) detector of 150 eV resolution. To reduce significantly the Compton scattering, improve the fluorescence/scattering ratio, and lower detection limits, this detector was shielded with a Cu/Mo collimator and set in the plane of the synchrotron ring, perpendicular to the incoming beam. The energy window in which the fluorescence could be detected varied from the low-energy background of the detector (1 keV) to the energy of the incident beam (15 and 22 keV,

Table 2. Calculated concentrations of samples GG20 and GG15 using Cl content of a saturated NaCl liquid (26 equivalent wt.% NaCl) as an internal standard (in ppm).

Sample GG20

Inclusion	E_i	K	Ca	Ti	Mn	Fe	Cu	Zn	As	Br	Rb	Sr	Ba	Pb
2g	15	10,526 ± 527	42,020 ± 777	285 ± 104	608 ± 21	3,301 ± 70	7 ± 2	462 ± 13		123 ± 5			2,245 ± 272	55 ± 19
2g	15	9,289 ± 495	35,883 ± 746		1,172 ± 37	4,465 ± 104	5 ± 2	356 ± 12	34 ± 13	103 ± 5			2,059 ± 292	
5c	15	6,078 ± 184	25,557 ± 312	92 ± 32	436 ± 9	1,800 ± 26	2 ± 0.5	273 ± 5	40 ± 6	76 ± 2			1,351 ± 90	38 ± 9
6i′	15	5,365 ± 405	32,805 ± 433	146 ± 45	1,296 ± 17	4,669 ± 47	4 ± 1	395 ± 5	49 ± 6	113 ± 2			1,845 ± 128	68 ± 9
6j′	15	13,203 ± 916	63,135 ± 909	400 ± 94	583 ± 14	5,642 ± 69	7 ± 1	668 ± 10	20 ± 5	183 ± 3			3,164 ± 260	23 ± 9
6i	15	6,132 ± 196	28,524 ± 354	80 ± 32	227 ± 6	911 ± 16	3 ± 1	302 ± 5	37 ± 6	81 ± 2			1,607 ± 96	47 ± 9
6i′	22	5,919 ± 1009	28,061 ± 890	15 ± 10	840 ± 35	4,794 ± 127	9 ± 1	380 ± 13		110 ± 0.3	123 ± 0.3	1,829 ± 2	1,268 ± 382	457 ± 1
6j′	22	28,797 ± 13612	30,674 ± 4,675		1,490 ± 239	5,227 ± 502	13 ± 3	249 ± 40						
Sample	mean	10,664	35,832	170	831	3,851	6	385	36	113	123	1,829	1,934	115
GG20	σ	7,831	12,183	145	447	1,698	4	134	10	35			649	169

Sample GG15

Inclusion	E_i	K	Ca	Ti	Cr	Mn	Fe	Cu	Zn	Br	Rb	Sr	Pb
5f	15	7,817 ± 186	9,241 ± 142	262 ± 22	64 ± 6	4,141 ± 46	33,084 ± 271		375 ± 6	41 ± 1			241 ± 8
5f	15	59,307 ± 1251	64,506 ± 948	1,242 ± 118	387 ± 32	22,134 ± 250	169,543 ± 1441	10 ± 7	1,906 ± 30	194 ± 6			1,242 ± 43
5f	15	44,471 ± 885	43,397 ± 629	742 ± 73	128 ± 15	12,305 ± 143	89,817 ± 772		1,103 ± 18	125 ± 4			674 ± 25
4e	15	41,632 ± 999	54,580 ± 862	809 ± 96	115 ± 18	9,891 ± 143	119,240 ± 1121	10 ± 7	498 ± 14	77 ± 5			363 ± 31
8i	15	33,169 ± 945	44,117 ± 715	2,286 ± 137	158 ± 20	14,063 ± 166	106,622 ± 896		1,474 ± 23	148 ± 5			914 ± 36
8i	15	47,100 ± 999	54,539 ± 753	1,506 ± 105	318 ± 24	18,842 ± 192	212,118 ± 1570		1,302 ± 19	115 ± 4			770 ± 27
9j	15	50,483 ± 692	48,583 ± 554	663 ± 57	108 ± 13	8,867 ± 99	121,306 ± 910		605 ± 11	84 ± 3			432 ± 20
5f	22	26,484 ± 800	28,168 ± 513	272 ± 59	13 ± 2	8,301 ± 110	83,738 ± 754	11 ± 2	784 ± 16	102 ± 4	358 ± 7	1,216 ± 16	848 ± 17
5f	22	11,555 ± 344	11,207 ± 201	124 ± 23	15 ± 2	2,486 ± 33	27,370 ± 241	2 ± 0.3	252 ± 5	32 ± 1	113 ± 2	389 ± 5	275 ± 5
4e	22	10,712 ± 786	13,000 ± 422	170 ± 50		1,598 ± 45	23,739 ± 358		62 ± 6	16 ± 2	62 ± 3	136 ± 5	87 ± 6
Sample	mean	33,273	37,134	807	145	10,263	98,658	8	836	93	177	580	585
GG15	σ	18,364	20,245	695	128	6,767	61,638	4	593	55	158	565	363

E_i incident beam energy (keV).

Table 3. Calculated concentrations of samples GG20 and GG15 using synthetic fluid inclusions containing 19.6 wt.% $CaCl_2$, as an external standard (in ppm).

Sample GG20

Inclusion	E_i	Cl	K	Ca	Ti	Mn	Fe	Cu	Zn	As	Br	Ba	Pb
2g	15	150,500 ± 5,800	10,055 ± 504	40,140 ± 743	272 ± 99	581 ± 20	3,153 ± 67	7 ± 2	441 ± 12		117 ± 4	2,145 ± 260	52 ± 18
2g	15	88,600 ± 2,900	5,226 ± 279	20,188 ± 420		659 ± 21	2,512 ± 59	3 ± 1	200 ± 7	19 ± 7	58 ± 3	1,159 ± 164	
5c	15	238,300 ± 4,600	9,193 ± 278	38,656 ± 472	139 ± 48	659 ± 13	2,722 ± 39	3 ± 1	412 ± 7	61 ± 9	115 ± 3	2,043 ± 137	57 ± 13
6i′	15	361,100 ± 29,500	12,298 ± 927	75,196 ± 993	335 ± 103	2,970 ± 39	10,702 ± 108	8 ± 1	904 ± 12	113 ± 13	259 ± 4	4,228 ± 294	157 ± 19
6j′	15	176,600 ± 19,000	14,805 ± 1,027	70,792 ± 1,019	448 ± 106	654 ± 16	6,327 ± 78	8 ± 1	749 ± 11	23 ± 6	205 ± 4	3,548 ± 292	26 ± 10
6i	15	303,900 ± 6,700	11,830 ± 379	55,024 ± 682	154 ± 62	439 ± 11	1,757 ± 30	5 ± 1	582 ± 10	71 ± 11	156 ± 3	3,099 ± 186	90 ± 17
Sample	mean	219,833	10,568	49,999	270	994	4,529	6	548	57	152	2,704	77
GG20	σ	101,255	3,263	21,010	129	972	3,413	2	253	39	72	1,125	50

Sample GG15

Inclusion	E_i	Cl	K	Ca	Ti	Cr	Mn	Fe	Cu	Zn	Br	Pb
5f	15	513,800 ± 8,100	25,461 ± 606	30,101 ± 464	854 ± 71	207 ± 18	13,488 ± 148	107,764 ± 884		1,221 ± 18	132 ± 4	785 ± 26
5f	15	86,400 ± 2,800	32,491 ± 686	35,340 ± 519	680 ± 65	212 ± 17	12,126 ± 137	92,884 ± 790	5 ± 4	1,044 ± 16	106 ± 4	681 ± 23
5f	15	142,000 ± 3,900	40,037 ± 797	39,070 ± 567	668 ± 65	116 ± 14	11,078 ± 129	80,862 ± 695		993 ± 16	113 ± 4	607 ± 23
4e	15	82,200 ± 2,400	21,710 ± 521	28,462 ± 450	422 ± 50	60 ± 10	5,158 ± 75	62,181 ± 585	5 ± 4	260 ± 7	40 ± 2	189 ± 16
8i	15	104,400 ± 3,900	21,948 ± 626	29,192 ± 473	1512 ± 91	105 ± 13	9,306 ± 110	70,551 ± 593	±	976 ± 16	98 ± 3	605 ± 24
8i	15	145,800 ± 4,900	43,553 ± 923	50,432 ± 696	1393 ± 97	294 ± 23	17,423 ± 178	196,144 ± 1,451	±	1,204 ± 18	106 ± 4	712 ± 25
9j	15	178,500 ± 2,600	57,130 ± 783	54,980 ± 627	750 ± 65	122 ± 15	10,034 ± 112	137,278 ± 1,030	±	685 ± 12	95 ± 4	489 ± 23
Sample	mean	179,014	34,619	38,225	897	159	11,230	106,809	5	912	99	581
GG15	σ	151,697	13,112	10,659	403	81	3,792	46,697	0	338	29	197

E_i incident beam energy (keV) .

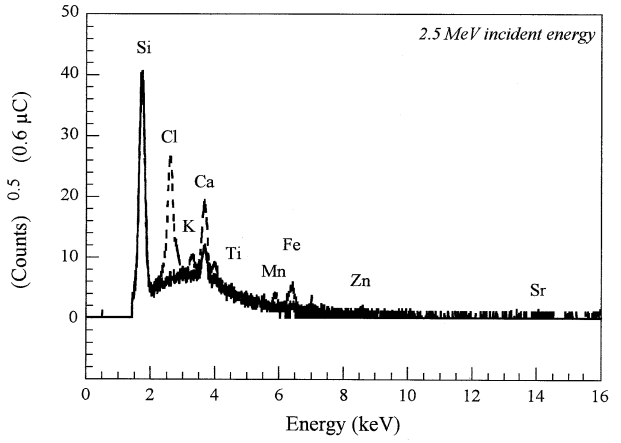

Fig. 6. PIXE spectrum of a fluid inclusion (i.e., 6i′) from Chivor emerald deposit, Columbia. Two spectra are overlaid: spectrum obtained on the fluid inclusion (broken line) and a control spectrum obtained in the nearby free-inclusion quartz (solid line). The X-ray spectrum reveals the presence of Cl, K, Ca, Mn, Fe, Cu, Zn, above the background noise and restricted solely to the inclusion. Si and Ca derived from the host quartz and from the sample holder, respectively.

respectively). The distance between the sample and the detector was 20 mm. The fluid inclusion samples were mounted on rigid silica glass microcapillaries positioned on a goniohead that suspended the samples in air.

Single analyses were recorded with an acquisition time of 10 to 15 min. Scans for trace element distribution of single fluid inclusions were performed using a 1 min per step integration time. To subtract any counts not arising from the inclusion, control spectra were systematically performed on nearby inclusion-free matrix and repeated when experimental conditions were modified. Before each analysis, two orthogonal scans with 10 s per step acquisition time were carried out over an area spanning the inclusion for different elements of interest, to select the point of maximum count rate in the inclusion. Furthermore, for a precise positioning of the sample in the beam, images based on phase contrast were collected on fluid inclusions with a high-resolution Charge-Coupled Device (CCD) camera placed behind the sample (Fig. 4).

4.2. Micro-PIXE

The PIXE experiments were carried out using the proton beam arising from the 3.75-MV Van de Graaff accelerator of the Pierre Süe laboratory nuclear microprobe (Commissariat à l'Energie Atomique, Saclay, France). The 2.5-MeV proton beam was accelerated through the beamline and focused by conventional beam optics to the first angular collimator of the microprobe. The object spot formed by the collimator was concentrated by a magnetic quadrupole doublet (Heidelberg type) to a beam spot size of $15 \times 15\ \mu m^2$ on the target. The incident beam direction was normal to the sample surface. A solid-state Si(Li) X-ray detector with a resolution of 160 eV at 5.9 keV was placed at 45° with respect to the incoming beam. The detector, covered with a 3-mm-diameter collimator, was placed at 30 mm to maximize the solid angle and hence the counting rate for the less numerous high-energy X-rays. The detector was also masked with a Mylar absorber, nominally 52 μm, to heavily attenuate the intense low-energy X-rays and to allow higher beam current to be applied without overloading the detector. For quantitative measurements, the beam current was monitored. The samples were surface coated with carbon (15 nm) to ensure reliable beam current integration and protect the target surface from charging during measurement and thereby avoid a high "Bremsstrahlung" background over the whole spectrum. A maximum integrated charge of 2 μC was deposited on the sample (typically 0.6 μC) with a beam current intensity varying from 600 to 800 pA (acquisition time of ~10 min.). The mineral plate containing the inclusions of interest was mounted over a 16-mm-diameter hole between two stretched films of 6-μm-thick Mylar and fitted onto an X-Y-Z mobile stage, enclosed in a high vacuum analytical chamber. The mineral plate was illuminated from the back side by a fiber optic illuminator, thus allowing observation in transmitted light. The front side of the sample facing the proton beam was observed using a video camera associated with a microscope.

5. RESULTS

Eleven fluid inclusions in quartz from samples GG15 and GG20 were analyzed by SXRF using two different incident energies of 15 and 22 keV. Figure 5 shows two typical SXRF

Table 4. Results of PIXE analysis on samples GG20 and GG15 (in ppm).

Inclusion	E_i	K	Ca	Ti	Mn	Fe	Zn
Sample GG20							
2f	2,500	53,941 ± 2,109	62,411 ± 1872		3,053 ± 555	15,008 ± 882	4,233 ± 693
5c	2,500	6,935 ± 183	30,417 ± 319	349 ± 53	295 ± 45	1,513 ± 73	527 ± 70
6i′	2,500	3,739 ± 1,101	20,856 ± 1,208		782 ± 354	17,108 ± 1,068	710 ± 570
6l	2,500	6,405 ± 383	28,929 ± 538	447 ± 149	1,322 ± 138	4,677 ± 226	925 ± 156
	mean	17,755	35,653	398	1,363	9,577	1,599
	σ	24,164	18,326	70	1,202	7,643	1,764
Sample GG15							
2b	2,500	20,992 ± 422	33,275 ± 516	223 ± 127	4,906 ± 224	96,683 ± 977	2,530 ± 254
3c	2,500	40,608 ± 524	50,734 ± 619	177 ± 114	10,559 ± 295	86,491 ± 891	2,861 ± 256
3d	2,500	24,566 ± 489	19,629 ± 440		5,981 ± 243	139,548 ± 1,172	1,448 ± 223
	mean	28,722	34,546	200	7,149	107,574	2,280
	σ	10,448	15,591	33	3,002	28,155	739

E_i incident beam energy (keV).

Table 5. Comparison between independent SXRF and PIXE analysis performed on the same fluid inclusions from sample GG20 (in ppm).

Inclusion 5c (GG20)							
Analytical method		K	Ca	Ti	Mn	Fe	Zn
SXRF	Cl from a 26 wt% equivalent NaCl liquid	6,078 ± 184	25,557 ± 312	92 ± 32	436 ± 9	1,800 ± 26	273 ± 5
PIXE	Ca from synthetic fluid inclusions	9,193 ± 278	38,656 ± 472	139 ± 48	659 ± 13	2,722 ± 39	412 ± 7
		6,935 ± 183	30,417 ± 319	349 ± 53	295 ± 45	1,513 ± 73	527 ± 70
Inclusion 6i′ (GG20)							
Analytical method		K	Ca	Ti	Mn	Fe	Zn
SXRF	Cl from a 26 wt.% equivalent NaCl liquid	5,365 ± 405	32,805 ± 433	146 ± 45	1,296 ± 17	4,669 ± 47	395 ± 5
PIXE	Ca from synthetic fluid inclusions	12,298 ± 927	75,196 ± 993	335 ± 103	2,970 ± 39	10,702 ± 108	904 ± 12
		3,739 ± 1,101	20,856 ± 1,208		782 ± 354	17,108 ± 1,068	710 ± 570

spectra obtained using 15- and 22-keV incident energies for the same fluid inclusion from sample GG20, located ~12 μm below the sample surface. Different X-ray lines (K-lines for light elements and L-lines for Ba and Pb, respectively) are measured. Because the majority of the fluorescence events arise from photons with energy just above the considered absorption edge, the sensitivity is optimized for elements displaying X-ray fluorescence lines just below the monochromatic excitation energy. Using 22 keV incident energy results in maximizing the sensitivity of heavy transition elements ($Z > 35$) and to a lesser extent that of Pb and lighter transition elements. Note also how Sr, with a critical excitation energy of 16.1 keV, is detected solely with a 22 keV incident energy. For light elements such as Cl, K, and Ca, a lower incident energy (15 keV in the present study) is better adapted.

Determination of elemental peak areas was achieved using the program WinAxil (Vekemans et al., 1994, 1995). The contribution of the host mineral and the experimental environment (i.e., Cu/Mo collimator in particular) was taken into account in each fluid inclusion analysis through the control spectrum (Fig. 5). The information relevant to the X-ray absorption by the host mineral was directly extracted from each spectrum using the (Kα/Kβ) ratio method (Philippot et al., 1998). Measured intensities were corrected using Ca Kα and Kβ X-rays. Ca was chosen because both Kα and Kβ X-rays are well discriminated in energy and are not overlapped by other X-rays, thus displaying peak area fits of good quality. Moreover, because low-energy X-ray yields are more sensitive to absorption, the Kα/Kβ ratio of a light element such as Ca gives more precise depth estimates than higher Z elements ($Z > 25$). Considering that the X-ray absorption induced by the fluid itself is one order of magnitude lower than that of the host mineral, the fluid inclusion thicknesses were measured optically using a spindle stage (Philippot et al., 1998). Finally, the elemental concentrations have been estimated using the mathematical treatment described in Ménez (1999).

5.1. Cl as Internal Standard

Considering that the fluid inclusions of both samples are saturated with respect to halite and that they have been targeted in their liquid portion, a salinity of 26 wt.% equivalent NaCl was assumed for evaluating the Cl content of the liquid phase. Establishing that the Cl Kα X-ray peak intensity corresponds to a concentration of 157,800 ppm provides one means of estimating the concentrations of the other elements present in solution. Results of the calculations are presented in Table 2. Note that, because large inclusions have been targeted in different locations, several measurements can be attributed to one inclusion.

5.2. Synthetic Fluid Inclusions of Known $CaCl_2$ Content Used as External Standard

As Ca is very common in most natural fluids and is also suitable for absorption correction purposes (i.e., Kα/Kβ method), aqueous fluid inclusions containing 19.6 wt.% $CaCl_2$ were synthesized in a fractured quartz crystal within gold capsules at high temperature and pressure (700°C and 0.7 GPa). Concentration estimates calculated using the Ca content of synthetic fluid inclusions are shown in Table 3. Because the excitation energy for synthetic and natural fluid inclusion measurements has to be identical, calculations were restricted to analysis performed using a 15-keV photon beam. As a consequence Rb and Sr concentrations are not determined. For each analyzed fluid inclusion, Ca concentration was estimated by comparison with the known Ca content in the synthetic inclusion, following the procedure described in Ménez (1999). Calculated Ca concentrations in samples GG15 and GG20 are in relatively good agreement with crush-leach analysis with a standard deviation of 42% and 28% of the mean value for samples GG20 and GG15, respectively. Establishing that the Ca Kα X-ray peak intensity corresponds to the Ca content, determined for each inclusion, Ca was used in turn as an internal standard to

Table 6. Calculated concentrations of samples GG20 and GG15 using mean Ca content deduced from PIXE analysis, as an external standard (in ppm).

Sample GG20

Inclusion	E_i	Cl	K	Ti	Mn	Fe	Cu	Zn	As	Br	Rb	Sr	Ba	Pb
2g	15	133,700 ± 5,200	8,931 ± 447	242 ± 88	516 ± 18	2,801 ± 60	6 ± 2	392 ± 11		104 ± 4			1,905 ± 231	46 ± 16
2g	15	156,500 ± 5,100	9,230 ± 492		1,164 ± 37	4,436 ± 104	5 ± 2	354 ± 12	34 ± 13	102 ± 5			2,046 ± 290	
5c	15	219,800 ± 4,300	8,479 ± 256	128 ± 44	608 ± 12	2,511 ± 36	3 ± 1	380 ± 7	56 ± 8	106 ± 2			1,884 ± 126	53 ± 12
6i′	15	171,200 ± 14,000	5,831 ± 440	159 ± 49	1,408 ± 18	5,074 ± 51	4 ± 1	429 ± 6	54 ± 6	123 ± 2			2,005 ± 139	74 ± 9
6j′	15	89,000 ± 9,600	7,456 ± 517	226 ± 53	329 ± 8	3,186 ± 39	4 ± 1	377 ± 6	12 ± 3	103 ± 2			1,787 ± 147	13 ± 5
6i	15	196,900 ± 4,300	7,665 ± 245	100 ± 40	284 ± 7	1,138 ± 20	3 ± 1	377 ± 6	46 ± 7	101 ± 2			2,008 ± 120	59 ± 11
6i′	22	200,100 ± 26,900	7,521 ± 1,282	19 ± 13	1,067 ± 45	6,090 ± 161	11 ± 2	483 ± 17		140 ± 0.4	157 ± 0.4	2,324 ± 2	1,611 ± 486	581 ± 1
6j′	22	183,100 ± 63,700	33,472 ± 15,822		1,732 ± 278	6,076 ± 584	16 ± 3	289 ± 47						
6i	22		8,522 ± 2,816		3,211 ± 488	10,151 ± 1038		805 ± 126		275 ± 203	4,430 ± 1,956			
Sample	mean	168,788	10,790	146	1,147	4,607	7	432	40	111	216	3,377	1,892	138
GG20	σ	41,973	8,566	83	921	2,670	4	150	18	15	84	1,489	153	218

Sample GG15

Inclusion	E_i	Cl	K	Ti	Cr	Mn	Fe	Cu	Zn	Br	Rb	Sr	Pb
5f	15	589,600 ± 9,300	29,221 ± 695	980 ± 81	238 ± 21	15,479 ± 170	123,678 ± 1014		1,401 ± 21	152 ± 5			901 ± 29
5f	15	84,500 ± 2,800	31,761 ± 670	665 ± 63	207 ± 17	11,854 ± 134	90,798 ± 772	5 ± 4	1,021 ± 16	104 ± 3			665 ± 23
5f	15	125,600 ± 3,400	35,401 ± 704	590 ± 58	102 ± 12	9,795 ± 114	71,498 ± 615		878 ± 14	99 ± 3			536 ± 20
4e	15	99,800 ± 2,900	26,350 ± 632	512 ± 61	73 ± 12	6,260 ± 91	75,472 ± 709	6 ± 4	315 ± 9	49 ± 3			230 ± 20
8i	15	123,500 ± 4,600	25,973 ± 740	1,790 ± 108	124 ± 16	11,012 ± 130	83,491 ± 701		1,154 ± 18	116 ± 4			716 ± 28
8i	15	99,900 ± 3,300	29,834 ± 632	954 ± 67	201 ± 16	11,935 ± 122	134,359 ± 994		825 ± 12	73 ± 2			488 ± 17
9j	15	112,200 ± 1,600	35,896 ± 492	471 ± 41	77 ± 9	6,305 ± 71	86,256 ± 647		430 ± 8	60 ± 2			307 ± 15
5f	22	193,400 ± 7,300	32,481 ± 981	334 ± 72	15 ± 3	10,180 ± 135	102,698 ± 924	13 ± 2	962 ± 19	126 ± 5	439 ± 9	1,491 ± 20	1,040 ± 21
5f	22	486,200 ± 13,500	35,619 ± 1061	383 ± 72	46 ± 7	7,662 ± 103	84,372 ± 742	5 ± 1	778 ± 15	97 ± 4	348 ± 7	1,198 ± 16	849 ± 16
4e	22	419,100 ± 28,000	28,466 ± 2,089	451 ± 134		4,247 ± 119	63,087 ± 953		165 ± 15	42 ± 5	164 ± 9	363 ± 12	231 ± 16
Sample	mean	233,380	31,100	713	120	9,473	91,571	7	793	92	317	1,017	596
GG15	σ	189,473	3,730	438	78	3,362	22,620	4	386	35	140	585	287

E_i incident beam energy (keV).

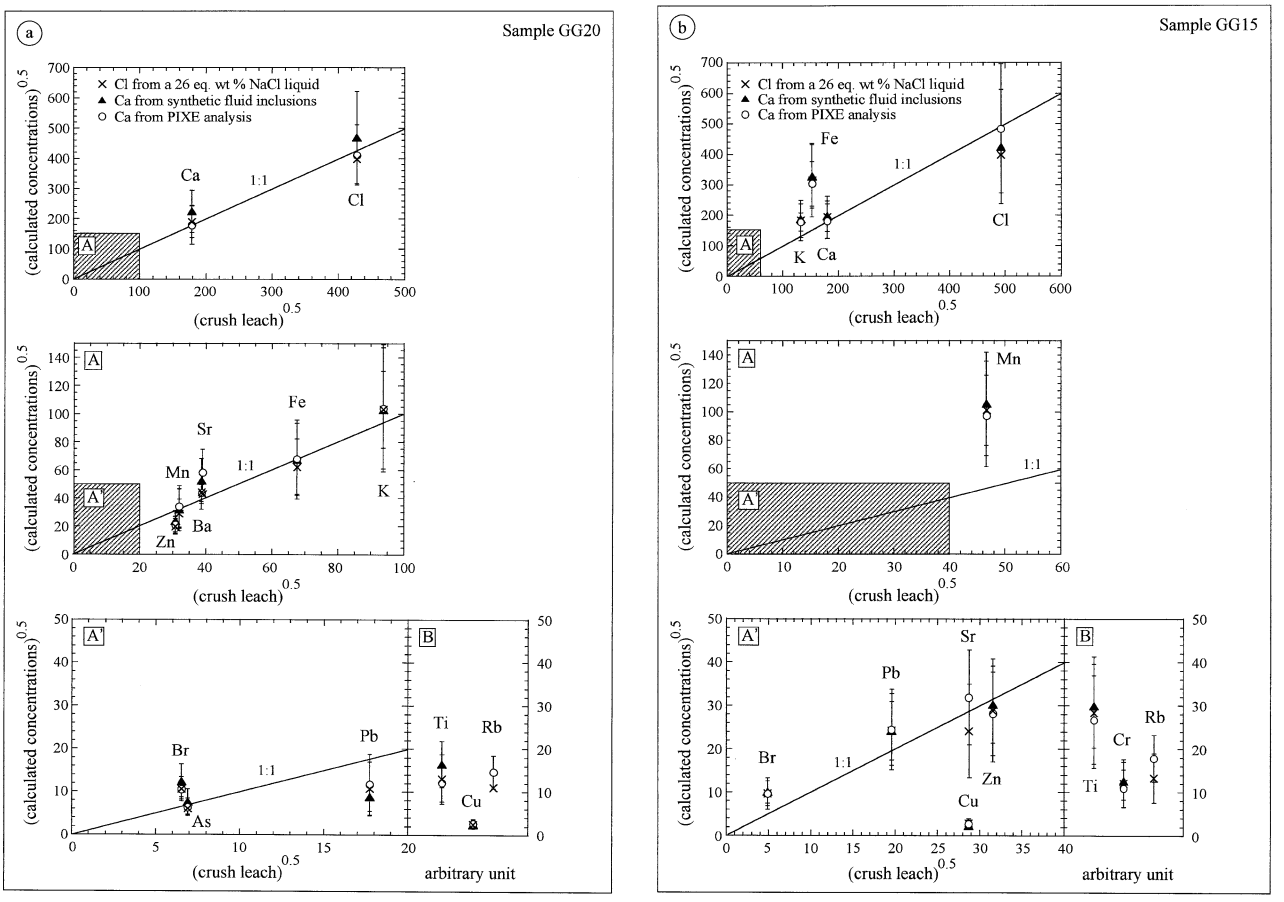

Fig. 7. Mean calculated concentrations and associated standard deviation from fluid inclusions in samples GG20 [5a] and GG15 [5b] obtained using the different calibration procedures. The zone B corresponds to elements not detected or analyzed by crush leach.

calculate the concentrations of the other elements present in the X-ray spectrum.

5.3. PIXE Analysis

Figure 6 shows a typical X-ray spectrum obtained on a fluid inclusion from sample GG20 using a 2.5-MeV proton beam and an integrated charge of 0.6 μC. Note the presence of a marked Cl and Ca peak and several less developed peaks corresponding to K, Ti, Mn, Fe, and Zn. In contrast to SXRF analysis, high-Z elements (from Br to Pb) were not detected using PIXE analysis. The calculation of elemental concentrations was carried out using GUPIX software (Maxwell et al., 1989). The fluid inclusion is modeled as a thin film of saline brine of fixed thickness and infinite lateral extent. Considering the greater size of the particle beam compared to SXRF analysis, and to target the liquid portion of the fluid inclusions, only large inclusions displaying a minimum size of 20 μm were analyzed. Assuming that both analyses were performed on the same location, thicknesses of quartz above the inclusion (i.e., fluid inclusion depth) are deduced from the Kα/Kβ ratios obtained for the SXRF analysis of the same fluid inclusions. As for SXRF analysis, fluid inclusion thicknesses were optically determined using a spindle stage. Table 4 shows quantitative compositional data obtained for K, Ca, Ti, Mn, Fe, and Zn, using the Cl content (26 wt.% equivalent NaCl = 157,800 ppm) of the saturated liquid portion of the inclusion as internal standard.

Note that for the first time, identical fluid inclusions were successfully analyzed by both techniques. Indeed, as highlighted in Table 5, inclusion GG20-5c and inclusion GG20-6i′ were the subject of experiments at both facilities. Although the correspondence is not perfect, the results present no gross systematic problems between both SXRF and PIXE analyses, performed independently.

Owing to the high sensitivity of the nuclear microprobe for light element detection (see section 2), chlorine is generally well characterized using PIXE technique. Consequently, independent PIXE analysis may provide an alternative mode for calibrating SXRF spectrum, especially in the case of low-salinity fluid analysis. This approach has been tested here, following the protocol detailed hereafter. Chlorine from microthermometry was used as an internal standard for quantifying low- to medium-Z elements in the PIXE spectrum, including Ca. Mean Ca concentration deduced from PIXE analysis was in turn used for quantifying heavy trace metals from the SXRF spectra. The concentration estimates, presented in Table 6, are

Table 7. Relative discrepancies (%) calculated by comparing the mean concentrations, obtained using the different calibration procedures for samples GG20 and GG15, with the crush-leach analysis.

Sample GG20											
Calibration procedure	Cl	K	Ca	Mn	Fe	Zn	As	Br	Sr	Ba	Pb
Cl from a 26 equivalent wt% NaCl liquid	*−14*[a]	+21	+12	−19	−16	−59	−25	+164	+20	+27	−63
Ca from synthetic fluid inclusions	+20	+20	+57[a]	−3	−1	−42	+19	+255		+80	−76
Ca from PIXE analysis	−8	+23	*+12*[a]	+12	+0.6	−55	−17	+159	+122	+26	−56
Crush leach (ppm)	183,208	8,796	31,855	1,025	4,579	950	48	42.8	1,524	1,503	315

Sample GG15										
Calibration procedure	Cl	K	Ca	Mn	Fe	Cu	Zn	Br	Sr	Pb
Cl from a 26 equivalent wt% NaCl liquid	*−35*[a]	+91	+15	+372	+324	−99	−16	+291	−30	+53
Ca from synthetic fluid inclusions	−26	+99	*+18*[a]	+416	+359	−99	−9	+316		+52
Ca from PIXE analysis	−4	+79	+7[a]	+335	+294	−99	−20	+287	+23	+56
Crush leach (ppm)	242,078	17,415	32,356	2,176	23,252	825	997	23.8	825	383

[a] Relative errors on the standard concentration used to calibrate the SXRF spectrum.

in accordance with the results obtained previously (see Tables 2 and 3).

5.4. Comparison with Crush-Leach Analysis

Figure 7 shows the mean concentration values obtained for both samples using the different calibration procedures as a function of the element concentrations determined by crush-leach analysis. Concentration estimates of Ti, Cu, and Rb, which were not analyzed or below the detection limits of the crush-leach analysis, are also shown. Several important observations may be made. First, considering that no a priori selection has been made on the set of data, the standard deviation of all measurements derived from all the calibration procedures is large (up to 98% of the mean value in both samples, and 159% in the specific case of Pb in sample GG20). Concentration estimates based upon the Cl content of a liquid phase saturated in NaCl show the largest scatter. Second, in contrast to the standard deviation, the mean concentration values of each element obtained independently with the different calibration procedures are very similar. Third, as shown in Table 7, with the exception of Zn, Br, Sr, and Pb in sample GG20, and K, Mn, Fe, Cu, and Br in sample GG15, mean concentration estimates are in good agreement with crush-leach analysis. On average, the procedure employing the Ca concentration extracted from PIXE analysis yields mean concentration values most comparable to crush-leach data. Note that Zn and Pb in sample GG20 and Cu in GG15 display mean values that are significantly lower than the crush-leach determination. Conversely, Br and Sr in GG20 and K, Mn, Fe, and Br in GG15 present much higher mean values. SXRF analysis of sample GG15 yields much higher concentrations for Mn and Fe than the crush-leach analysis. Nevertheless, this disagreement for both elements is confirmed by PIXE analysis. No explanation for this large difference in Mn and Fe concentrations can be proposed, however. The apparent discrepancy for Cu and Br in sample GG15 and Zn, Br, and Pb in sample GG20 is discussed below in light of elemental distribution results.

5.5. Elemental Distributions

Figure 8 shows the elemental distribution in a single fluid inclusion of sample GG15. The *x-y* scan was performed using a $2 \times 7\ \mu m^2$ beam spot size and an integration time of 70 s per step. Owing to the shape of the beam spot, the vertical resolution of the maps is one order of magnitude higher than the horizontal resolution. For each point of the map, which corresponds to an individual X-ray fluorescence spectrum, the $K\alpha/K\beta$ ratio of Ca was used to estimate the pathlength through quartz of the fluorescent radiation. This value was in turn used to correct each X-ray spectrum for absorption. Because the horizontal dimension of the beam was significantly larger than the size of the daughter crystals, absorption by the solid phases was not taken into account. As a consequence, distribution maps of the light elements (Cl and K), which are more sensitive to X-ray absorption (Fig. 1), are poorly constrained. In addition, using a short acquisition time of 70 s compared to 10 min for concentration estimates, implies that light elements such as Cl and K will be hardly detectable. Importantly, note that the SXRF maps were performed at 45° to the wafer surface but that the fluid inclusion image was obtained using conventional transmitted light microscopy. This implies that both images cannot strictly overlap.

To facilitate the discussion of the results, the analyzed fluid inclusion was divided into different regions schematically represented in the bottom right panel of Figure 8. With the exception of Pb and Br, all elements show the highest count rates in region A of the inclusion where the daughter crystals are

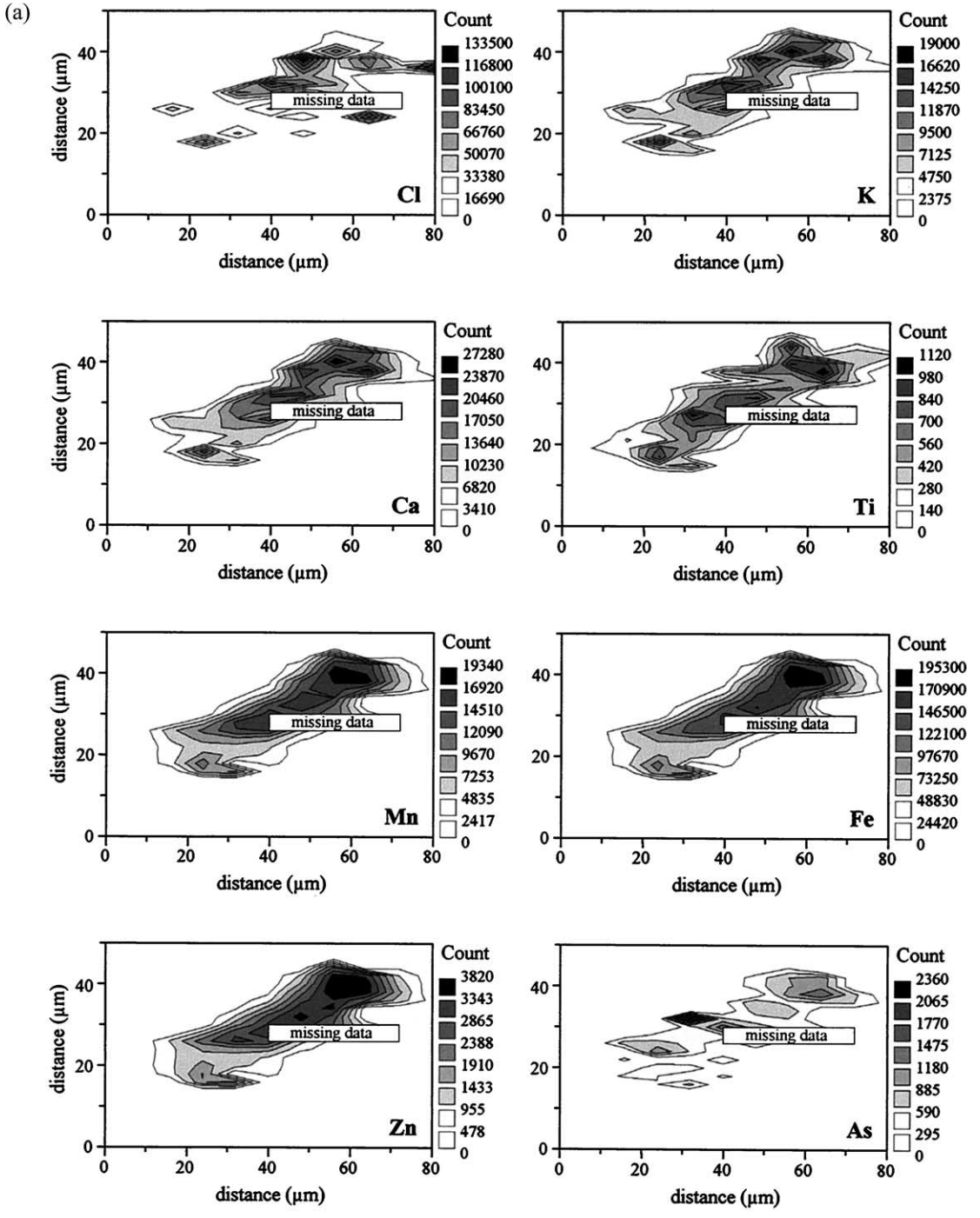

Fig. 8. Elemental distribution in a single fluid inclusion from Guali emerald deposit (GG15). Maps were constructed using a 70 s per step integration time, a 15 keV incident energy, and a beam spot size of 2×10 μm^2 and were corrected for host-mineral absorption using the Kα/Kβ ratio method. For discussion, the fluid inclusion is divided into different regions schematically represented in the bottom right panel. Region A (hatched zone) coincides with the position of the daughter crystals. Region B (plain white zone) corresponds to the liquid portion of the inclusion. The vapor bubble is localized in region C (shaded zone).

located. Mn, Fe, and Zn all display a uniform distribution throughout the inclusion. Ba, As, Ti, and Pb display clusters but have relatively regular distributions in the liquid portion of the inclusion (region B). Pb shows the highest count rates away from the daughter-crystal-rich area. In contrast to the other elements, Br shows a relatively low count rate in region B of the inclusion (i.e., liquid portion) but an unusually high count rate in region C that corresponds to the location of the vapor bubble. These observations are best illustrated in the correlation diagrams shown in Figure 9.

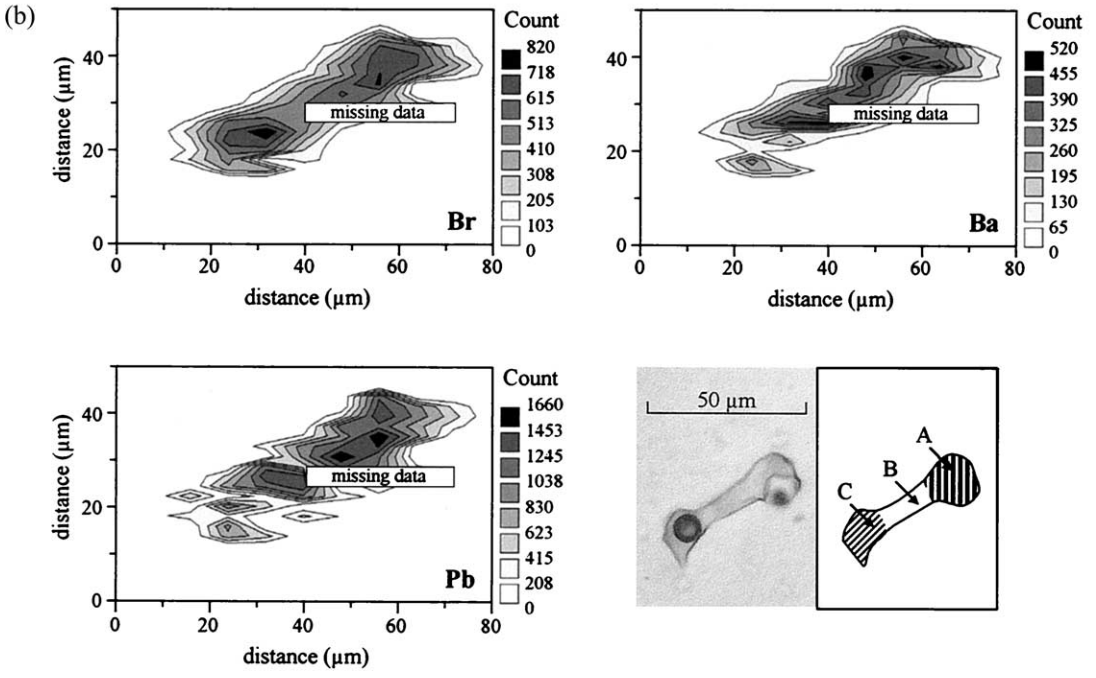

Fig. 8. (Continued)

The perfect correlations between Fe, Zn, and Mn, presented in Figure 9a, indicate that these elements are distributed in the same proportions throughout the inclusion (see Somogyi et al., 2000, for the interpretation of interelement correlation graphs). Similar good correlations have been recorded for Ca, K, and Ba and to a lesser extent for Ti and Pb. With regard to Cu and As (Fig. 9b), note that the two elements show a relatively high correlation coefficient of 0.81 and one point, which is discussed below, displays a much higher count rate than the average. In contrast, the distribution of Br displays two types of linear correlation with all the elements present in the fluid inclusion (Fig. 9c). This, together with recognition that Br exhibits a relatively high count rate in the vapor portion of the inclusion (Fig. 8) strongly argues for a strong presence of Br into the vapor phase, in contrast with the other elements. These results are discussed below in light of some experimental results and recent observations from ore deposits.

6. DISCUSSION AND PERSPECTIVES

Different important observations arise from the results presented above. Mean concentration estimates obtained with the different calibration procedures are in relatively good agreement with crush-leach analysis. Single irradiation of a fluid inclusion will obviously yield an analysis that is subject to quite large errors. However, averaging the results from a number of different inclusions belonging to a given population produces reliable results. The relatively large scattering of the measurements is caused partly by analytical uncertainties and by the complexity of the analyzed multiphase fluid inclusions. This also reflects to some extent fluid composition heterogeneities at the sample scale. Thus, obtaining a good Cl or Ca concentration for each inclusion, deduced from individual measurement instead of a mean value, may result in less scattering of the elemental concentration estimates.

Elemental distribution maps represent a powerful complementary tool for interpreting quantitative analysis. As an example, elemental correlation diagrams shown in Figure 9b provide constraints for elucidating the apparent discrepancy in Cu concentration estimates deduced from crush-leach analysis. Cu was undetected in sample GG20, in agreement with concentration estimates of 6 to 7 ppm deduced from SXRF measurements. However, in sample GG15, the crush-leach Cu concentration estimate of 825 ppm contrasts with results from SXRF analysis which yielded only 5 to 12 ppm Cu. A similar discrepancy can be recognized for As. In sample GG20, crush-leach and SXRF analysis yielded similar As concentration estimates of 48 ppm and 36 ppm to 57 ppm, respectively. But in sample GG15, although the crush-leach analysis gave an As content of 39 ppm, we were not able to detect any As using the SXRF technique. As seen in Figure 9b, both the low Cu and undetectable As in the liquid portion of the inclusion from GG15 may be explained by the presence of an optically invisible As- and Cu-bearing mineral. The localized high As count rate in Figure 9b may indicate the location of a tiny invisible mineral. During the crush-leach process, these tiny daughter minerals would have dissolved into the acid leachate solution. Although we did not perform any elemental mapping in sample GG20, recognition of systematically lower Zn and Pb concentrations (Fig. 7a) may be attributed to the presence of a Zn- and Pb-bearing phase.

Another important result of this study is the observation that vapor can contain significant amounts of Br. This supports the results of Heinrich et al. (1992), Ryan et al. (1993), and Damman et al. (1996) who demonstrated, using PIXE analysis,

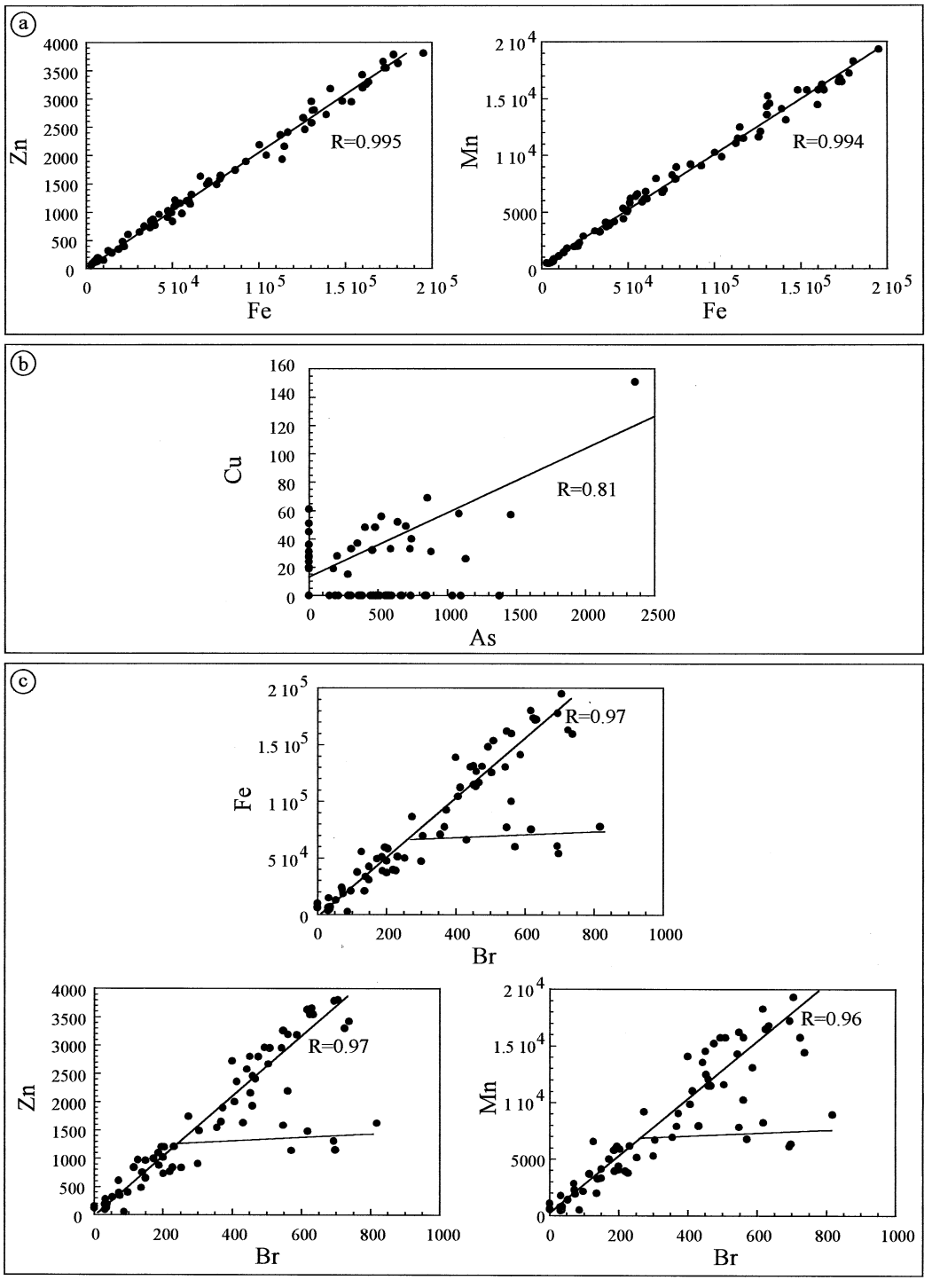

Fig. 9. Interelement correlation graphs established from the elemental spatial distribution of the fluid inclusion from Guali emerald deposit (GG15) presented in Figure 8. The correlation coefficients were calculated on all the data points.

the presence of metals, notably Cu, Fe, Cr, Zn, Mn, Pb, as well as Rb, Sr, and Br in vapor inclusions. Brine-vapor separation, which is highly element-specific, may be a major segregation mechanism leading to base and precious metals deposition in ore systems. Heinrich et al. (1992) showed that copper was complexed by a sulfur ligand in the vapor phase rather than chloride. Damman et al. (1996) suggested that Br complexing could be a way to extract elements from a high-salinity brine. We may find in this study support for this last suggestion. However, this point remains controversial. Oosting and Von Damm (1996) have clearly observed that Br stays preferentially in the liquid whereas Berndt and Seyfried (1990, 1997) present

experimental results showing the opposite. Further studies dedicated to this aspect would provide new information on bromine behavior in the crust and on metal transport and subsequent precipitation. X-ray fluorescence micro-tomography allowing one to obtain 3D elemental images of fluid inclusions (Ménez et al., 2001) would also be helpful to confirm the presence of bromine in the vapor phase.

The results presented in this study show that the ionic content of single fluid inclusions can be estimated by the different calibration procedures tested. A variety of standards (i.e., both external and internal) allows unrestricted quantitative analysis on a large variety of fluid inclusions. Indeed, Cl is ubiquitous and Ca occurs commonly in natural fluids. The use of synthetic fluid inclusions containing Ca appears to be a judicious choice because this element is sensitive to absorption and hence adapted to the ($K\alpha$/$K\beta$) ratio method. Moreover, Ca is also well suited for measurement standardization. The main advantage of these procedures is to finally allow quantitative analysis of metal concentrations in individual fluid inclusions without a precise knowledge of the analytical volume and the three-dimensional inclusion geometry. It is obvious that these methods are better suited to biphase fluid inclusions (i.e., liquid and vapor phases) or homogenized fluids. Consequently, any application to less saline and less heterogeneous inclusion fluids should be optimized. Nevertheless, as in the present case, the relative complexity of multiphase fluid inclusions can be circumvented by analyzing the liquid portion of the inclusion and performing several analyses (about 10) for the same population of fluid inclusions.

The highly intense source provided by the ESRF is ideally suited for tracking and mapping a large variety of trace metals in individual fluid inclusions. The geochemistry of trapped fluids by means of SXRF analysis must finally be considered as a new exploration tool providing unique information for an improved understanding of rock-forming processes and of mechanisms and conditions controlling the transport and the concentration of economic resources in the Earth's crust (Ménez, 1999; Philippot et al., 2000; hydrocarbons, Foriel et al., 2000).

Acknowledgments—We thank Gaston Giuliani for kindly providing the samples analyzed in this study and Robert Burruss and David Vanko for their support and constructive comments on the manuscript. We acknowledge Anatoly Snigirev from μFID22 group (ESRF) for welcoming us, and Irina Snigireva for the use of the ESRF's micromanipulation facility. This work was funded by a BRGM Grant GéoFrance 3D to P. Philippot.

Associate editor: R. C. Burruss

REFERENCES

Banks D. A., Yardley B. W. D., Giuliani G., Cheilletz A., and Rueda F. (1995) Chemistry and source of the high temperature brines in the Colombian emerald deposits. In *Mineral Deposits: From Their Origin to Their Environmental Impacts* (eds. J. Pasava, B. Kribek, and K. Zak), pp. 557–560. Balkema, Rotterdam.

Banks D. A., Giuliani G., Yardley B. W. D., and Cheilletz A. (2000). Emerald mineralisation in Colombia: Fluid chemistry and the role of brine mixing. *Mineral. Deposita* **35,** 699–713.

Berndt M. E. and Seyfried W. E. (1990) Boron, bromine and other trace elements as clues to the fate of chlorine in mid-ocean ridge vent fluids. *Geochim. Cosmochim. Acta* **54,** 2235–2245.

Berndt M. E. and Seyfried W. E. (1997) Calibration of Br/Cl fractionation during subcritical phase separation of seawater: Possible halite at 9 to 10°N East Pacific Rise. *Geochim. Cosmochim. Acta* **61,** 2235–2245.

Bodnar R. J. (1995) Fluid inclusion evidence for a magmatic source for metals in porphyry copper deposits. In *Magmas, Fluids and Ore Deposits* (ed. J. H. F. Thompson), Short Course Series, **23,** pp. 139–152. Mineralogical Association of Canada.

Bühn B. and Rankin A. H. (1999) Composition of natural, volatile-rich Na-Ca-REE-Sr carbonatitic fluids trapped in fluid inclusions. *Geochim. Cosmochim. Acta* **63,** 3781–3797.

Cheilletz A. and Giuliani G. (1996) The genesis of Colombian emeralds: A restatement. *Mineral. Deposita* **31,** 359–364.

Chevallier P., Dhez P., Erko A., Firsov A., Legrand F., and Populus P. (1996) Hard X-ray microbeam production and application. *NIM B* **113,** 122–127.

Cline J. S. and Vanko D. A. (1995) Magmatically generated saline brines related to molybdenum at Questa, New Mexico, USA. In *Magmas, Fluids and Ore Deposits* (ed. J. H. F. Thompson), Short Course Series, **23,** pp. 153–174. Mineralogical Association of Canada.

Crawford M. L. (1981) Phase equilibria in aqueous fluid inclusions. In *Short Course in Fluid Inclusions: Applications to Petrology* (eds. L. S. Hollister and M. L. Crawford), **6,** 75–100. Mineralogical Association of Canada.

Damman A. H., Kars S. M., Touret J. L. R., Rieffe E. C., Kramer J. A. L. M., Vis R. D., and Pintea I. (1996) PIXE and SEM analysis of fluid inclusions in quartz crystals from the K-alteration zone of the Rosia Poieni porphyry-Cu deposit, Apuseni Mountains, Rumania. *Eur. J. Mineral.* **8,** 1081–1096.

Foriel J., Philippot P., Ménez B., Bonnin-Mosbah M., Simionovici A., and Walgenwitz F. (2000). Individual fluid inclusion analysis as a tool for predicting permeability barrier in oil reservoir. *7th Int. Conf. Nuclear Microprobe Technology and Applications*, Bordeaux, France. 105 (abstr.).

Frantz J. D., Mao H. K., Zhang Y. G., Wu Y., Thompson A. C., Underwood J. H., Giauque R. D., Jones K. W., and Rivers M. L. (1988) Analysis of fluid inclusions by X-ray fluorescence using synchrotron radiation. *Chem. Geol.* **69,** 235–244.

Giuliani G., Cheilletz A., Arboleda C., Carrillo V., Rueda F., and Baker J. (1995) An evaporitic origin of the parent brines of the Colombian emeralds: Fluid inclusions and sulfur isotopes evidence. *Eur. J. Mineral.* **7,** 151–165.

Giuliani G., France-Lanord C., Zimmermann J. L., Cheilletz A., Arboleda C., Charoy B., Coget P., Fontan F., and Giard D. (1997) Fluid composition, δD of channel H_2O, and $\delta^{18}O$ of lattice oxygen in beryls: Genetic implications for Brazilian, Colombian, and Afghanistani emerald deposits. *Int. Geol. Rev.* **39,** 400–424.

Heinrich C. A., Ryan C. G., Mernagh T. P., and Eadington P. J. (1992) Segregation of ore metals between magmatic brine and vapor: A fluid inclusion study using PIXE microanalysis. *Econ. Geol.* **87,** 1566–1583.

Mavrogenes J. A., Bodnar R. J., Anderson A. J., Bajt S., Sutton S. R., and Rivers M. L. (1995) Assessment of uncertainties and limitations of quantitative elemental analysis of individual fluid inclusions using synchrotron X-ray fluorescence (SXRF). *Geochim. Cosmochim. Acta* **59,** 3987–3995.

Maxwell J. A., Campbell J. L., and Teesdale W. J. (1989) The Guelph PIXE software package. *NIM B* **43,** 218–230.

Ménez B., Philippot P., Mosbah M., Drakopoulos M., and Snigirev A. (1998a) Individual fluid inclusion analysis combining PIXE, PIGE and synchrotron X-ray fluorescence (SXRF). *6th Int. Conf. Nuclear Microprobe Technology and Applications*, Spier Estate, Stellenbosh, South Africa. I3 (abstr.).

Ménez B., Philippot P., Vanko D., Mosbah M., Chevallier P., Drakopoulos M., Populus P., and Snigirev A. (1998b) Individual fluid inclusion microanalysis combining proton-induced and photon-induced X-ray emission (PIXE and SXRF). *7th PACROFI*, Las Vegas, 44 (abstr.).

Ménez B. (1999) Les microsondes photon et proton appliquées à l'analyse ponctuelle d'inclusions fluides: Un outil pour reconstituer l'évolution des paléosystèmes hydrothermaux [Individual fluid inclusion microanalysis combining proton and photon microprobes: A

tool for reconstructing paleohydrothermal processes]. Ph. D. thesis, Paris VII Univ.

Ménez B., Simionovici A., Philippot P., Bohic S., Gibert F., and Chukalina M. (2001). A first insight into X-ray fluorescence microtomography of an individual fluid inclusion using a third generation synchrotron light source. *NIM B* **181** (1–4), 749–754.

Mernagh T. P. and Wilde A. R. (1989) The use of the laser Raman microprobe for the determination of salinity in fluid inclusions. *Geochim. Cosmochim. Acta* **53,** 765–771.

Oosting S. E. and Von Damm K. L. (1996) Bromine/chloride fractionation in seafloor hydrothermal fluids from 9–10°N East Pacific Rise. *Earth Planet. Sci. Lett.* **144,** 133–145.

Ottaway T. L., Wicks F. J., Bryndzia L. T., Kyser T. K., and Spooner E. T. C. (1994) Formation of the Muzo hydrothermal deposit in Colombia. *Nature* **369,** 552–554.

Philippot P., Chevallier P., Chopin C., and Dubessy J. (1995) Fluid composition and evolution in coesite-bearing rocks (Dora-Maira massif, Western Alps): Implications for element recycling during subduction. *Contrib. Mineral. Petrol.* **121,** 29–44.

Philippot P., Ménez B., Chevallier P., Gibert F., Legrand F., and Populus P. (1998) Absorption correction procedures for quantitative analysis of fluid inclusions using synchrotron radiation X-ray fluorescence. *Chem. Geol.* **144,** 121–136.

Philippot P., Ménez B., Simionovici A., Chabiron A., Cuney M., Snigirev A., and Snigireva I. (2000) X-ray imaging of uranium in individual fluid inclusions. *Terra Nova* **12,** 84–89.

Philippot P., Ménez B., Drakopoulos M., Simionovici A., and Snigirev A. (2001) Mapping trace-metal (Cu, Zn, As) distribution in a single fluid inclusion using a 3rd generation synchrotron light source. *Chem. Geol.* **173,** 151–158.

Rankin A. H., Ramsey M. H., Coles B., Van Langevelde F., and Thomas C. R. (1992) The composition of hypersaline, iron-rich granitic fluids based on laser-ICP and synchrotron-XRF microprobe analysis of individual fluid inclusions in topaz, Mole granite, eastern Australia. *Geochim. Cosmochim. Acta* **56,** 67–79.

Ryan C. G., Cousens D. R., Heinrich C. A., Griffin W. L., Sie S. H., and Mernagh T. P. (1991) Quantitative PIXE microanalysis of fluid inclusions based on a layered yield model. *NIM B* **54,** 292–297.

Ryan C. G., Heinrich C. A., and Mernagh T. P. (1993) PIXE microanalysis of fluid inclusions and its application to study ore metal segregation between magmatic brine and vapor. *NIM B* **77,** 463–471.

Snigirev A. (1995) The recent development of Bragg-Fresnel optics: Experiments and applications at the ESRF. *Rev. Sci. Instr.* **66,** 2053–2058.

Snigirev A., Kohn V., Snigireva I., and Lengeler B. (1996) A compound refractive lens for focusing high energy X-rays. *Nature* **384,** 49–51.

Somogyi A., Vincze L., Janssens K., Vekemans B., Rindby A., and Adams F. (2000). Interpretation and use of inter-element correlation graphs obtained by scanning X-ray fluorescence micro-beam spectrometry from individual particles: Part I - theory. *Spectrochim. Acta* **55B,** 75–89.

Vanko D. A. and Mavrogenes J. A. (1998) Synchrotron-source X-ray fluorescence microprobe: Analysis of fluid inclusions. In *Applications of Microanalytical Techniques to Understanding Mineralizing Processes. Reviews in Economic Geology* (eds. M. A. McKibben and W. C. Shanks), **6,** 251–263

Vanko D. A., Sutton S. R., Rivers M. L., and Bodnar R. J. (1993) Major-element ratios in synthetic fluid inclusions by synchrotron X-ray fluorescence microprobe. *Chem. Geol.* **109,** 125–134.

Vanko D. A., Bonnin-Mosbah M., Philippot P., Roedder E., and Sutton S. R. (2001). Fluid inclusions in quartz from oceanic hydrothermal specimens and the Bingham, Utah, porphyry-Cu deposit: A study with PIXE and SXRF. *Chem. Geol.* **173,** 227–238.

Vekemans B., Janssens K., Vincze L., Adams F., and Van Espen P. (1994) Analysis of X-ray spectra by iterative least squares (AXIL): New developments. *X-Ray Spectrom.* **23,** 278–285.

Vekemans B., Janssens K., Vincze L., Adams F., and Van Espen P. (1995) Comparison of several background compensation methods useful for evaluation of energy-dispersive X-ray fluorescence spectra. *Spectrochim. Acta* **50B**, 149–169.